An Efficient and Stable Embedded Multi-U-Shaped Column Rotary Transformer

Yufei Zhou, *Member, IEEE*, Yang Luo, Shuai Liu, and Dongdong Li

***Abstract*—Inductively coupled power transfer (ICPT) technology can be used to solve the problems of high friction loss, overheating and low stability caused by conductive slip rings on rotating power supply equipment. An improved embedded multi-U-shaped column rotary transformer (EMUCRT) based on the ICPT and spliced core structure is proposed in this article. It has a higher coupling coefficient and can transmit power more efficiently and stably due to the primary magnetic core is embedded inside the secondary magnetic core. Compared with the one-piece core structure, the spliced type is more flexible due to its loose magnetic core arrangement. Its primary coil can still transmit energy stably after offset by a certain distance, so the structure has good anti-misalignment ability. On the basis of analyzing its magnetic core arrangement and magnetic circuit model, the optimal magnetic core specifications and quantities of primary and secondary side are obtained by theoretical calculation and simulation. In order to verify the high efficiency, rotational stability and anti-misalignment characteristics of the structure, an experimental prototype was built. The results show that EMUCRT can transmit energy efficiently and has good rotational and offset stability.**

***Index Terms*—Coupling coefficient, inductively coupled, magnetic circuit model, rotary transformer, rotational stability.**

I. Introduction

With the progress of society and the development of science and technology, rotating electrical equipment has gradually become an irreplaceable part in the industrial field. Traditional electrical joints between static and rotatable parts of automatic machines are realized by sliding contacts, such as the manipulators of the cranes [1]. Solar array drive assembly in the solar power supply system controls the rotation of the solar array through the rotation of the conductive slip ring, so that it can be directly irradiated by the sun, and can transmit the electric power and signal to the battery [2], [3], [4]. At present, the power supply of rotating equipment mainly uses conductive slip rings to electrically connect the fixed side and rotating side [5], [6]. However, in the actual working process of the conductive slip ring, due to the brush and the conductive ring transfer energy through contact, the long-term friction increases the loss of the element, and risks of fire and overheating, thus it reduces the reliability and safety. When working outdoors in rainy days, problems such as short circuit and metal oxidation corrosion caused by rainwater are easy to occur. At the same time, in order to improve the reliability as much as possible, precious metals such as gold, silver, and platinum are usually used as friction contacts of conductive slip rings, which are expensive [7]. Therefore, the inductively coupled power transfer (ICPT) technology provides a way to solve the problems for the power supply of the conductive slip ring [8]. By applying ICPT technology to rotating equipment, a contactless rotary transformer structure is proposed [9], [10], and [11]. The structure has the characteristics of contactless transmission of electric energy, high coupling coefficient, and diversified application occasions, so it greatly extends the lifetime of the equipment, increases the reliability, safety and waterproofness of the power supply, and reduces the production cost [12], [13], [14], [15].

Contactless rotary transformers are mainly divided into two types: tank type and column type. The structural feature of the tank structure is that the coils are filled in the grooves in the magnetic core, and the two magnetic cores are placed relatively for rotation. Since there is a certain distance between the primary and secondary coils, energy can be transmitted contactlessly, and the primary and secondary sides can rotate freely. Thus its structure increases the freedom and reliability of the transformer, but it is inefficient and cumbersome [16]. In view of the problem that the integral tank-type transformer is bulky and not easy to carry, some scholars have proposed a spliced tank-type rotary transformer core structure. This structure greatly reduces the number and weight of magnetic cores, and it is easy to carry and assemble [5], [6], [17]. In order to improve the coupling coefficient and efficiency of the spliced tank-type magnetic core, splicing-type rotary transformers with high-frequency ferromagnetic materials and litz-wire are proposed in [18], experiments show that high power and efficient energy transmission is realized. Based on the column-type, a separable column transformer is designed [19]. This structure cuts the entire magnetic column inside and outside, thereby reducing the electrical conductivity in the magnetic core and reducing the eddy current loss. The final experimental results show that the system has a maximum efficiency of 84.4% under the condition of 2 mm air-gap. However, this structure simply divides the magnetic core, and does not fundamentally reduce the amount of magnetic core, so the weight of the transformer will not be reduced. In order to meet the requirements of lightweight

Manuscript received 14 July 2022; revised 27 September 2022, 24 November 2022, and 9 January 2023; accepted 26 January 2023. Date of publication 16 February 2023; date of current version 10 March 2023. Recommended for publication by Associate Editor M. Ponce-Silva . *(Corresponding author: Yufei Zhou.)*

The authors are with the College of Electronic and Information Engineering/College of Integrated Circuits, Nanjing University of Aeronautics and Astronautics, Nanjing 211100, China (e-mail: zhou_yufei@126.com; 1025934518@qq.com; 1291638010@qq.com; lucaslidd@163.com).

Color versions of one or more figures in this article are available at https://doi.org/10.1109/TPEL.2023.3243211.

Digital Object Identifier 10.1109/TPEL.2023.3243211

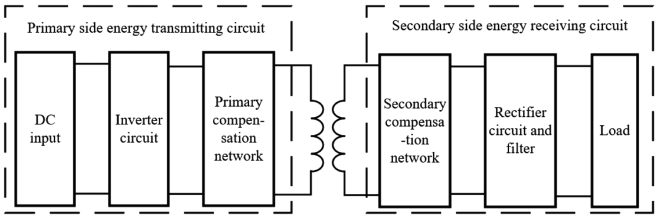

Fig. 1. Block diagram of inductively coupled rotary transformer system.

system and further improve the transmission efficiency, a spliced column structure composed of strip-shaped small magnetic cores distributed on the coils is proposed [20]. The structure retains the characteristics of the column structure. The method of attaching the magnetic strip greatly reduces the amount of the integral magnetic core, and improves the coupling coefficient of the transformer, so that the efficiency of the whole machine can reach 87.1%.

In order to realize high efficiency and stable energy transmission of the contactless rotary transformer, this article proposes an embedded multi-U-shaped column rotary transformer (EMUCRT) structure. Compared with the traditional column transformer, the embedded magnetic core structure makes the secondary magnetic core wrap the primary magnetic core. This not only effectively improves the coupling coefficient of the transformer and increases the transmission efficiency of the system, but also makes the primary magnetic core less susceptible to external damage when it rotates internally, which improves the stability of the physical structure. The spliced magnetic core structure greatly reduces the electrical conductivity of the magnetic core by reducing the amount of magnetic cores, and significantly reduces the eddy current loss. In practical application, it not only reduces the weight and improves the portability of the transformer, but also increases the heat dissipation area of the transformer. Only a single core needs to be replaced when broken, which improving the reparability of the system. In order to verify the advantages of the structure proposed, the remaining of the article is structured as follows. Section II introduces the inductively contactless rotary transformer system. Section III introduces the spliced multi-U-shaped column rotary transformer (SMUCRT) structure. In order to improve the coupling coefficient of the spliced magnetic core, the EMUCRT is proposed in Section IV. In the Section V, the EMUCRT experiment is conducted to verify its performance. Compared with the SMUCRT, it has higher transmission efficiency, better offset and rotational stability. Finally, Section VI concludes this article.

II. Inductively Coupled Rotary Transformer System

The inductively coupled rotary transformer system is mainly composed of three parts, namely the energy transmitting circuit of primary side, the energy receiving circuit of secondary side and the contactless rotary transformer. The system block diagram is shown in Fig. 1.

The energy transmitting circuit of the primary side is mainly composed of a dc regulated power supply, an inverter circuit and a compensation network. The main function of the compensation network is to compensate for the leakage inductance of the transformer, thereby increasing the output power and output efficiency. The energy receiving circuit of secondary side is mainly composed of compensation network, rectifier filter circuit and load. The function of the compensation network is the same as that of the primary side.

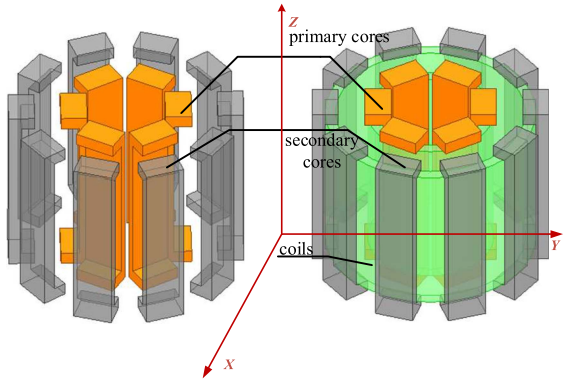

Fig. 2. Spliced multi-U-shaped column core structure.

The inductively coupled rotary transformer applies the principle of electromagnetic induction and transfers energy in a contactless way. The alternating current flows through the primary coil to generate an alternating magnetic field, and the induced electromotive force of secondary side is generated by alternating magnetic field, thereby energy is transferred from primary side to secondary side.

In the case of the same transformer specifications, the outer column of the column-type rotary transformer can converge the magnetic lines of force of the inner column more easily. Under the same simulation conditions of coil radius, turns and cross sections of the ferrite cores, the following conclusion is obtained through simulation research: When under the condition of keeping the coupling coefficient similar, the weight and volume of the column structure is lower than that of the tank structure. So we choose the column structure here for optimization.

III. Equivalent Magnetic Circuit Model and Parameters Design of SMUCRT

A. Width Design of Magnetic Core

Considering the disadvantages of using a magnetic core, such as small heat dissipation area, and poor system lightweight, the integral column-type rotary transformer should be divided into pieces. Fig. 2 shows the multi-U-shaped column core structure.

In a loosely coupled transformer with a large air-gap, magnetic lines of force will choose a path with relatively small magnetoresistance to circulate. Therefore, the magnetic lines of force will not only flow on the end face of the magnetic core, but also on the side and the corner of the magnetic core. Since the shape of the magnetic flux at the end face of the magnetic core is relatively regular, the magnetoresistance can be performed according to the standard equation [21]. However, at the corner and the side of the magnetic core, the flow path of the magnetic lines of force is extremely complex, and the shape of the magnetic flux

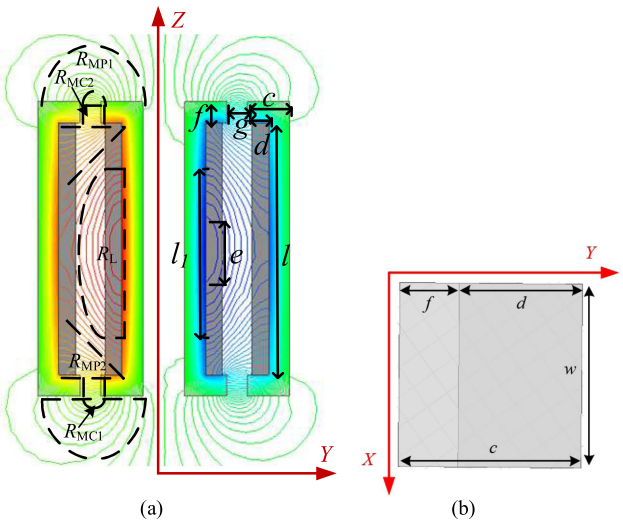

Fig. 3. (a) Schematic diagram of the distribution of magnetic lines of force of the 2-D cross section of *YZ*. (b) Schematic diagram of the *XY* plane of a single magnetic core.

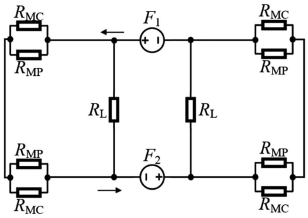

Fig. 4. Equivalent magnetic circuit model of SMUCRT.

is irregular. It is necessary to artificially divide the irregular magnetic flux into small modules of regular shape, and obtain the magnetoresistance according to the empirical equation. By dividing the three-dimensional (3-D) model in Fig. 2, taking its *YZ* section at the center position and the *XY* plane at the top of a single core for 2-D analysis, a schematic diagram of the distribution of magnetic lines of force and an *XY* cross section of single core are obtained, as shown in Fig. 3(a) and (b) [the grey ones in Fig. 3(a) are the coils].

According to the different coupling level, magnetic lines of force are divided into three regions, which are the complete coupling region, the incomplete coupling region and the completely uncoupled region. The magnetic flux of the complete coupling region is divided into two parts, which circulate through the magnetoresistance R_{MC1} and R_{MC2}, respectively. The magnetoresistance of the incomplete coupling region is R_{MP1} and R_{MP2}, and the magnetoresistance of the completely uncoupled region is R_L. According to the magnetoresistance shape, the magnetoresistance empirical equations are obtained [21], as given in Table I, where $\mu_0 = 4\pi \times 10^{-7}$ H/m in the empirical equation is the vacuum permeability.

The equivalent magnetic circuit model is obtained by region division, as shown in Fig. 4.

Combining the magnetic circuit model in Fig. 4 and the empirical equation in Table I, each magnetoresistance can be

TABLE I
MAGNETORESISTANCE MODEL AND CORREPONDING EMPIRICAL EQUATION

Magneto resistance	Empirical equation	legend
R_{MC1}	$\frac{1}{0.26\mu_0 w}$	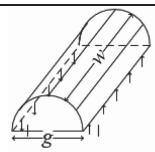
R_{MC2}	$\frac{g}{\mu_0 wf}$	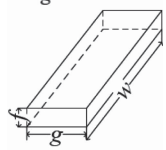
R_{MP1}	$\frac{\pi(\frac{g}{c}+1)}{2\mu_0 w}$	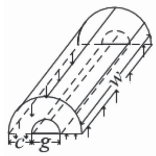
R_{MP2}	$\frac{4(g+2d)}{\mu_0 wl_1}$	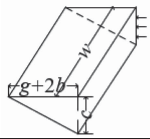

obtained as

$$R_{MC} = R_{MC1} \parallel R_{MC2} = \frac{\frac{1}{0.26\mu_0 w} \cdot \frac{g}{\mu_0 wf}}{\frac{1}{0.26\mu_0 w} + \frac{g}{\mu_0 wf}} \tag{1}$$

$$R_{MP} = R_{MP1} \parallel R_{MP2} = \frac{\frac{\pi(\frac{g}{c}+1)}{2\mu_0 w} \cdot \frac{4(g+2d)}{\mu_0 wl_1}}{\frac{\pi(\frac{g}{c}+1)}{2\mu_0 w} + \frac{4(g+2d)}{\mu_0 wl_1}}. \tag{2}$$

According to the simulation data, when the core length c of the rotary transformer is 15 mm, the structure has the advantages of high coupling coefficient, and its magnetic core quantity is small, which can meet the needs of lightweight. The air-gap between the primary and secondary side of the rotary transformer usually chooses 5 mm or more as a common size [6], [20]. For its wider application, take $g = 10$ mm as the air-gap of the structure. Since the structure in this article is used to replace the conductive slip ring to supply power to the equipment, its size is limited, and the outer diameter of the traditional conductive slip ring is usually about 20–100 mm. Considering the size and symmetry of the structure, combined with the scale and power level of the system, the diameter of the multiturn secondary coil in the horizontal direction is 90 mm, and that of the multi-turn primary coil is 70 mm after winding the coil, $d = 10$ mm, $f = 5$ mm, $l_1 = 45$ mm. By further taking the parameters into (1) and (2), the relationship between the magnetoresistance and the core width w can be obtained, as shown in Fig. 5.

It can be clearly seen from Fig. 5 that with the increase of the core width w, the magnetoresistance will decline obviously. But when the core width w increases to 15 mm, the decline trend of magnetoresistance slows down.

Since eddy current loss will be generated when alternating current is applied to the magnetic core, in order to ensure the

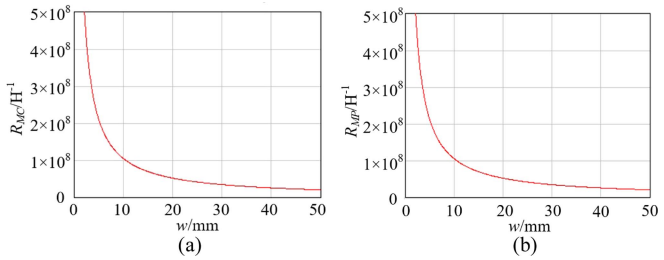

Fig. 5 Variation of the R_{MC} and R_{MP} with core width. (a) R_{MC}. (b) R_{MP}.

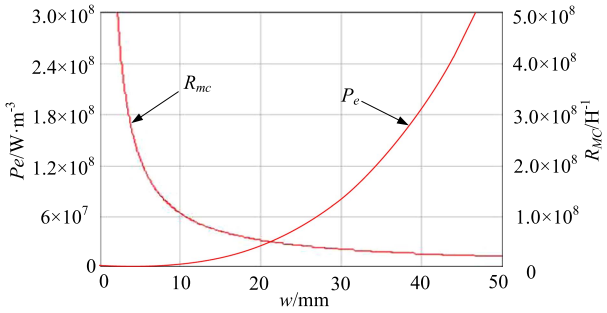

Fig. 6. Variation of the eddy current loss density and magnetoresistance with core width respectively.

optimal transmission efficiency of the transformer, the relationship between the width of the magnetic core and the eddy current loss should be considered. Assuming that the magnetic induction intensity B changes periodically with time, the time is denoted by t, and a square-section ferrite core with a length of c, a width of w, and a height of l. The calculation steps of the eddy current loss density are as follows [22], [23].

The instantaneous electromotive force around the core is

$$E(w,t) = cw\frac{dB}{dt}. \tag{3}$$

Its resistance value is

$$R = \rho\frac{c}{l{\cdot}dw} \tag{4}$$

where ρ is the resistivity. The power loss is

$$P(w,t) = \int \frac{E^2(w,t)}{R}d(w). \tag{5}$$

Taking (3) and (4) into (5), and integrating from $w = 0$ to w_0, the core power loss can be obtained as

$$P(t) = \frac{cl}{3\rho}w_0^3\left(\frac{dB}{dt}\right)^2. \tag{6}$$

The relationship between the voltage across the coil and the change in the magnetic induction of the magnetic core is

$$v(t) = N_1 cw\frac{dB}{dt} \tag{7}$$

where N_1 is the number of turns of the coil. Combining (6) and (7), the eddy current loss density of the square core can be obtained as

$$P_e = \frac{v^2(t)wl}{3N_1c^2\rho}. \tag{8}$$

When sinusoidal excitation is added: $v(t) = v_0\sin(\omega t)$and V_0 is the peak voltage. The peak magnetic induction intensity B_0 can be obtained according to (7)

$$B_0 = \frac{V_0}{N_1 cw\omega}. \tag{9}$$

The final eddy current loss density can be obtained by adding (7) and (9) into (8)

$$P_e = \frac{B_0^2\omega^2 w^3 cl}{3\rho}. \tag{10}$$

When the operating frequency is 100 kHz and under normal working conditions with a temperature of 25°, the B_0 of the ferrite core material is about 0.5T, and ρ is about 2 Ω·m, which is brought into the (10). The relationship curve between the core eddy current loss density P_e, magnetoresistance R_{MC} and the core width w are obtained in Fig. 6.

It can be seen from Figs. 5 and 6 that with the change of w, the magnetoresistance of the magnetic core tends to be stable in the range of 10–20 mm and the eddy current loss is low. Although continuing to increase the magnetic core width is beneficial to further reduce the magnetoresistance, the thicker the magnetic core selected, the higher the production cost, and it cannot meet the needs of lightweight. Then, the constraint range of w is brought into the simulation, and it is found that when the width of the magnetic core w is less than 10 mm, the coupling coefficient increases obviously, and when w exceeds 12 mm, the coupling coefficient of the transformer changes slowly. So the core width in the range of 12–20 mm is appropriate. Especially when the width of the magnetic core w increases from 12 to 15 mm, the coupling coefficient increases 0.037 per 57 g increased in weight. But when the width of the magnetic core w exceeds 15 mm, the coupling coefficient only increases by 0.02 for every 50 g increase in weight in the range of 15–20 mm. So we choose 15 mm as the final result.

B. Secondary Magnetic Core Gap

After the magnetic core width is determined, it is necessary to determine the gap length between the secondary magnetic cores. Taking the top view of SMUCRT shown in Fig. 3, a 2-D simulation of each magnetic core is performed, as shown in Fig. 7.

Since the distance between the two magnetic cores on the secondary side is short, in order to simplify the simulation and theoretical calculation, the arc paths l_a and l_b between the two magnetic cores are approximately taken as straight-line path h during the simulation, as is shown in Fig. 7

$$h = \frac{1}{2}(l_a + l_b). \tag{11}$$

By regularizing the leakage flux of the completely uncoupled region in Fig. 7(b), the empirical magnetoresistance equation of

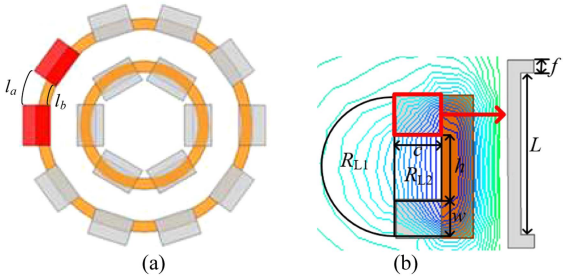

Fig. 7. Simulation diagram of the adjacent magnetic cores on the secondary side. (a) Top view of the rotary transformer. (b) 2-D simulation graph of adjacent magnetic cores.

TABLE II
MAGNETORESISTANCE MODEL AND CORRESPONDING EMPIRICAL EQUATION BETWEEN ADJACENT MAGNETIC CORES ON THE SECONDARY SIDE

Magneto-resistance	Empirical equation	legend
R_{L1}	$\frac{2(l+2f)}{\mu_0\pi(h+2w)}$	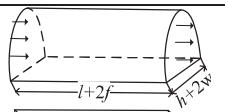
R_{L2}	$\frac{l+2f}{\mu_0 hc}$	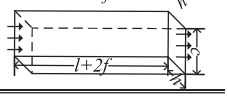

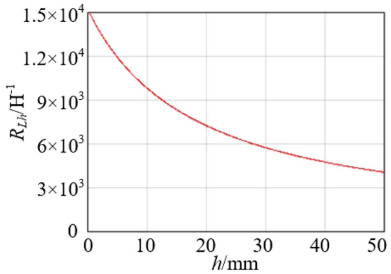

Fig. 8. Relationship between R_{Lh} and h.

the corresponding magnetic flux with regular shape is obtained, as given in Table II.

According to the magnetic circuit simulation results in Fig. 7 and the empirical equation in Table II, the R_{Lh} between two adjacent magnetic cores on the secondary side can be obtained:

$$R_{Lh} = R_{L1} \parallel R_{L2} = \frac{\frac{2(l+2f)}{\mu_0\pi(h+2w)} \cdot \frac{l+2f}{\mu_0 hc}}{\frac{2(l+2f)}{\mu_0\pi(h+2w)} + \frac{l+2f}{\mu_0 hc}}. \tag{12}$$

Taking the simulation parameters into (12), the relationship between the R_{Lh} and the length h can be obtained, as shown in Fig. 8.

Different from above R_{ML} and R_{MP}, R_{Lh} is completely uncoupled magnetoresistance, and the larger the value is, the more difficult it is for the magnetic lines to pass through this completely uncoupled region, and the more it can reduce the magnetic flux leakage. Therefore, the smaller the value of h, the better. But, if h is too small, more cores are needed to fill the gap, and the weight of the rotary transformer will increase. If h is too large, the leakage flux will increase, and the coupling coefficient will inevitably be greatly reduced. Since the perimeter of the

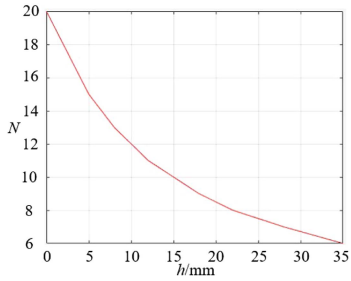

Fig. 9. Relationship between N and h.

secondary side has been fixed, and the specifications of the primary and secondary side magnetic cores are the same, in order to arrange the magnetic cores evenly, there is a certain relationship between the number of magnetic cores and the gap between the magnetic cores. Suppose the perimeter of the secondary side is c_s, the number of magnetic cores is N (N is an integer), and the gap between the secondary side magnetic cores is h, their relationship is as follows:

$$c_s = wN + hN. \tag{13}$$

According to (13), relationship between N and h is shown in the Fig. 9.

It can be seen from Fig. 9 that when h is in the range of 10–20 mm, the number of magnetic cores in the secondary side of the system is moderate. If h is less than 10mm, the number of magnetic cores required will increase significantly, and each 5 mm gap will increase about 3 cores, which will increase the weight of the transformer too much. When h is larger than 20 mm, the required number of cores will decrease, but the decreasing rate is low and the influence of overall weight is less important. Considering the data of Fig. 8 and Fig. 9, h is appropriate to choose 10 and 15 mm. When h is 10 mm, the number of cores is 12 and the coupling coefficient is 0.9. When h is 15 mm, the number of cores is 10, and the coupling coefficient is 0.896. There is little difference between the two coupling coefficients, and the effect on system efficiency can be ignored. In order to meet the demand of lightweight system, h is set as 15 mm and the number of secondary magnetic cores is 10.

IV. EQUIVALENT MAGNETIC CIRCUIT MODEL OF EMUCRT

In order to further improve the transmission efficiency of the SMUCRT, an EMUCRT is proposed. By increasing the length of the secondary magnetic core of the spliced rotary transformer, the primary magnetic cores are embedded inside the secondary magnetic cores. Fig. 10 is a full view and a top view of the EMUCRT. The secondary side rotates at the angle of θ in the Fig. 10(b) under normal working conditions. Compared with the SMUCRT mentioned in Section III, the primary and secondary magnetic cores of the embedded structure are more closely attached and lighter. At the same time, since the secondary side magnetic core wraps the primary magnetic cores, it can ensure that most of the magnetic field generated by the primary side is

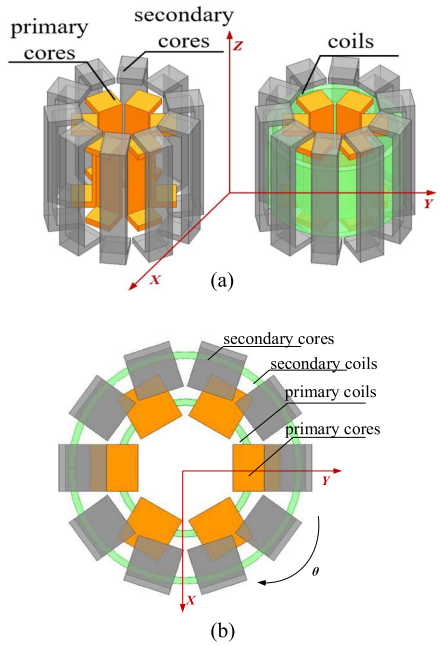

Fig. 10. Embedded multi-U-shaped column rotary transformer. (a) Full view. (b) Top view.

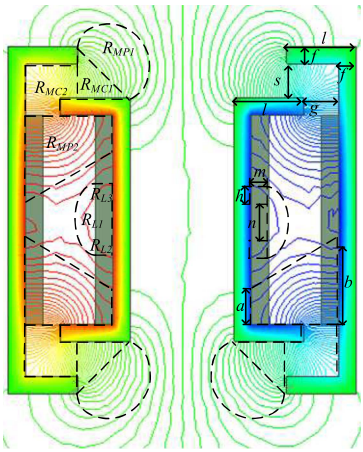

Fig. 11. Schematic diagram of magnetic lines of force in 2-D cross section.

received by the secondary side, which effectively improves the efficiency and stability of the system during rotation.

In order to investigate the distribution of the magnetic field, the structure in Fig. 10 is divided into the *YZ* plane and then a 2-D simulation is performed to investigate the direction of the magnetic lines of force, as shown in Fig. 11 (the grey ones are the coils).

By comparing the distributions of the magnetic lines of force in Figs. 3 and 11, due to the presence of embedded gap s, it can be seen that a part of the incomplete coupling region R_{MP1} in Fig. 3 is transformed into the completely coupled region R_{MC1} in Fig. 11. The area of the completely uncoupling region R_L is also partly reduced.

According to the division of the magnetic lines of force in Fig. 11, the construction of the magnetic circuit model is carried

TABLE III
MAGNETORESISTANCE MODEL OF THE STRUCTURE AND THE CORRESPONDING EMPIRICAL EQUATION

Magneto resistance	Empirical equation	legend
R_{MC1}	$\frac{2}{\mu_0 w}$	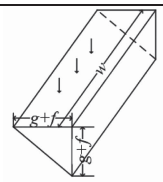
R_{MC2}	$\frac{s}{\mu_0 wf} \| \frac{g}{\mu_0 w(l-f)}$	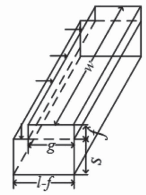
R_{MP1} R_{L1}	$\frac{1}{0.26\mu_0 w}$	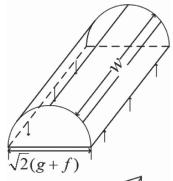
R_{MP2}	$\frac{2(g+2d)}{\mu_0 w(a+b)}$	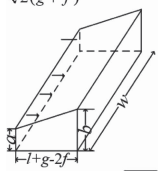
R_{L2} R_{L3}	$\frac{m}{\mu_0 wh}$	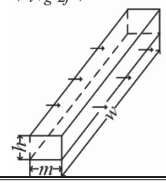

out. The magnetoresistance of the completely coupled region consists of two parts: R_{MC1}, R_{MC2}. The magnetoresistance of the incompletely coupled region is R_{MP1} and R_{MP2}. The magnetoresistance of the completely uncoupled region consists of three parts: R_{L1}, R_{L2}, and R_{L3}. According to the shape, the corresponding magnetoresistance empirical equation is obtained, as given in Table III.

The magnetoresistance in each region can be calculated according to the empirical equations. R_{MP} of the incomplete coupling region is obtained by connecting R_{MP1} and R_{MP2} in parallel, which can be expressed as

$$R_{MP} = R_{MP1} \parallel R_{MP2} = \frac{\frac{1}{0.26\mu_0 w} \cdot \frac{2(g+2d)}{\mu_0 w(a+b)}}{\frac{1}{0.26\mu_0 w} + \frac{2(g+2d)}{\mu_0 w(a+b)}}. \quad (14)$$

R_{MC} of the completely coupled region is obtained by connecting R_{MC1} and R_{MC2} in parallel, which can be expressed as

$$R_{MC} = R_{MC1} \parallel R_{MC2} = \frac{\frac{2}{\mu_0 w} \cdot \frac{\frac{s}{\mu_0 wf} \cdot \frac{g}{\mu_0 w(l-f)}}{\frac{s}{\mu_0 wf} + \frac{g}{\mu_0 w(l-f)}}}{\frac{2}{\mu_0 w} + \frac{\frac{s}{\mu_0 wf} \cdot \frac{g}{\mu_0 w(l-f)}}{\frac{s}{\mu_0 wf} + \frac{g}{\mu_0 w(l-f)}}}. \quad (15)$$

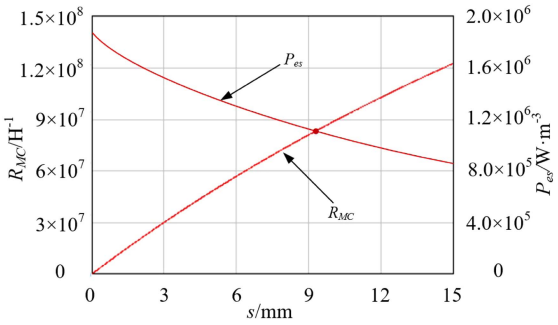

Fig. 12. Relationship between R_{MC}, P_{es}, and s.

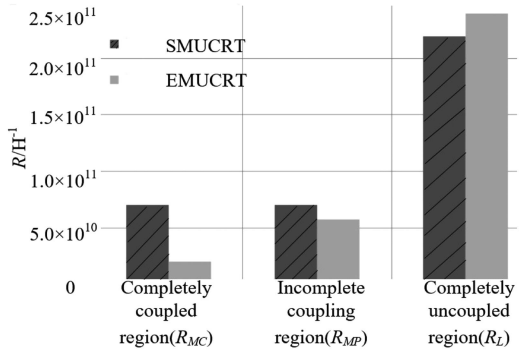

Fig. 13. Comparison of the magnetoresistance of SMUCRT and EMUCRT.

R_L of the completely uncoupled region is obtained by connecting R_{L1}, R_{L2}, and R_{L3} in parallel, which can be expressed as

$$R_L = R_{L1} \parallel R_{L2} \parallel R_{L3} = \frac{1}{0.26\mu_0 w} + 2\frac{m}{\mu_0 wh}. \tag{16}$$

The same as the parameters taken by the structure in the Section III, the physical parameters corresponding to the structure can be obtained as: $l = 15$ mm, $g = 10$ mm, $f = 5$ mm. Other parameters can be measured in 2-D simulation: $a = 15$ mm; $b = 25$ mm; $m = 5$ mm; and $h = 5$ mm. Bringing them into (15), the relationship between s and R_{MC} can be obtained. At the same time, the relationship between the eddy current loss density P_{es} and s can be obtained according to (10), which can be expressed as

$$P_{es} = \frac{B^2\omega^2 c^3 (80 - 2s)^3}{3\rho w}. \tag{17}$$

The relationship between R_{MC}, P_{es} and s are shown in Fig. 12.

It can be seen from Fig. 12 that when s increases, R_{MC} gradually increases, but the eddy current loss density declines. To sum up, take the intersection of the two curves in the Fig. 12 as the embedded gap, namely 10 mm. At this time, the incomplete coupling magnetoresistance is not large and the eddy current loss density is moderate.

When all parameters are determined, the magnetoresistance of the three coupling regions of SMUCRT and EMUCRT can be compared, as shown in Fig. 13.

Fig. 13 shows that the magnetoresistance of EMUCRT in the completely and incompletely coupled regions is significantly reduced, which is benefit for the transmission of magnetic lines of force from the primary side to the secondary side. In addition, the magnetoresistance of EMUCRT in the completely uncoupled region is significantly increased, which is beneficial to reduce the leakage of the magnetic lines of force and improve the coupling coefficient of the transformer. Therefore, the EMUCRT structure has a higher coupling coefficient.

TABLE IV
PARAMETERS OF EXPRIMENGTAL CIRCUIT

Parameters	Value/Model
Input voltage	V_{in}=100 V
Full load output power	P_o=100 W
Resonance frequency	f_0=100kHz
Inverter power devices	BSC350N20NSFDATM
Rectifier diode	C3D10065E
Material of cores	TDK PC40
Cores cross section	75mm^2
Material of windings	Litz Wire
Coil specifications	0.1 mm*150
Number of turns	12
Fixed method of Windings	Fixed with foam glue
Primary winding inductance	L_p=57.9μH
Secondary winding inductance	L_s=64.5μH
Primary compensation capacitor	C_p=289.4nF
Secondary compensation capacitor	C_s=40.1nF
Overall efficiency	η>90%

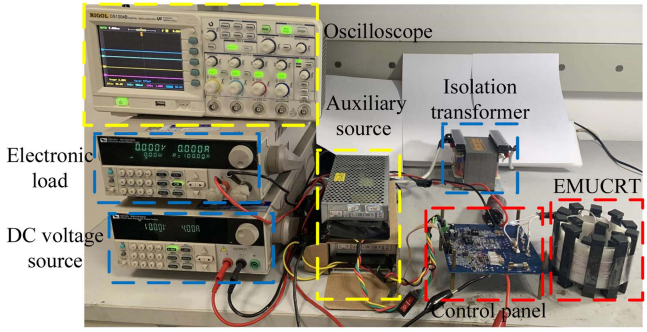

Fig. 14. EMUCRT experimental platform.

V. EXPERIMENTAL VERIFICATION

In order to verify the performance of the proposed EMUCRT, the circuit specifications and the main components and elements are given in Table IV. The experimental platform of inductive contactless rotary transformer based on S/P compensation network is built, as shown in Fig. 14.

The primary and secondary side compensation networks adopt S/P compensation, which is widely used in wireless power transfer (WPT) systems because of its simple structure and good transmission stability. The circuit diagram of the compensation network is shown in Fig. 15.

In Fig. 15, v_{in} and v_{out} are the input and output voltage of the compensation network. i_{in} and i_{out} are the input and output currents of the compensation network. L_p and L_s are the self-inductances of the primary and secondary coil windings, and C_p and C_s are the compensation capacitors of the primary side and the secondary side. R_p and R_s are the internal resistances on the primary and secondary coils, and M is the mutual inductance.

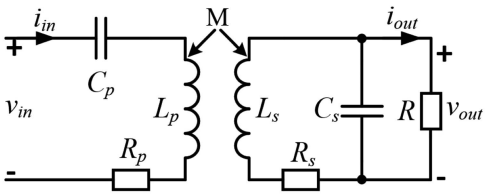

Fig. 15. S/P compensation circuit structure.

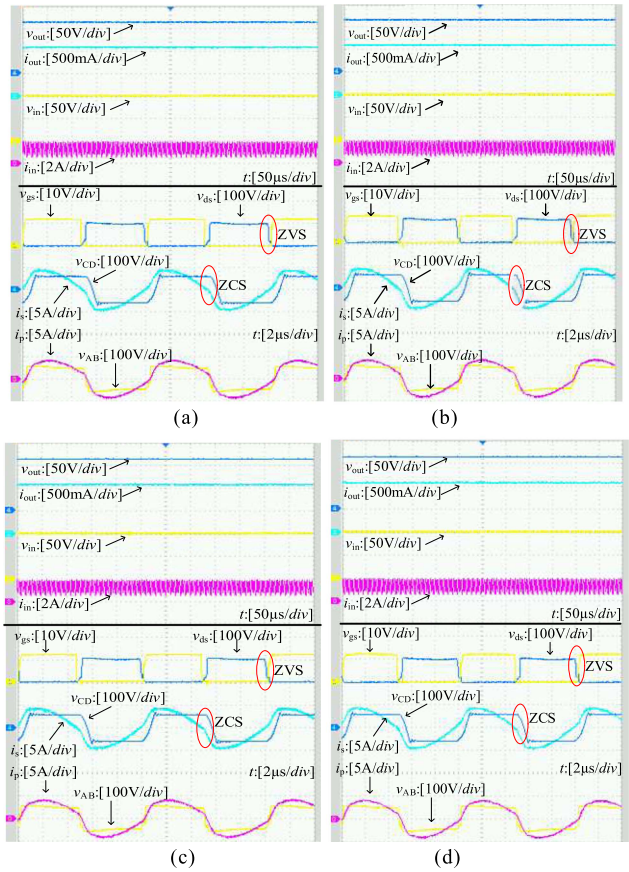

Fig. 16. Experimental waveforms of rotary transformer with different angular dislocations. (a) $\theta = 0°$. (b) $\theta = 60°$. (c) $\theta = 120°$. (d) $\theta = 180°$.

When the experiment is under full load, the key waveforms when the primary side is angularly rotated by an angle of θ are shown in Fig. 16, in which v_{gs} is the driving voltage of the upper MOSFET in the half-bridge inverter network, v_{ds} is the drain-source voltage of the switching devices, v_{AB} is the midpoint voltage of the bridge of the primary half-bridge inverter, i_p is the primary side resonant tank current, v_{CD} is the midpoint voltage of the bridge of the secondary side voltage doubling rectifier network, and i_s is the secondary side resonant tank current.

From the key waveforms of the transformer at different rotation angles in Fig. 16, it can be seen that zero-voltage-switching (ZVS) is realized on the primary side, and zero-current-switching (ZCS) is realized on the secondary side, which ensures that the system will not generate additional switching losses during the rotation process.

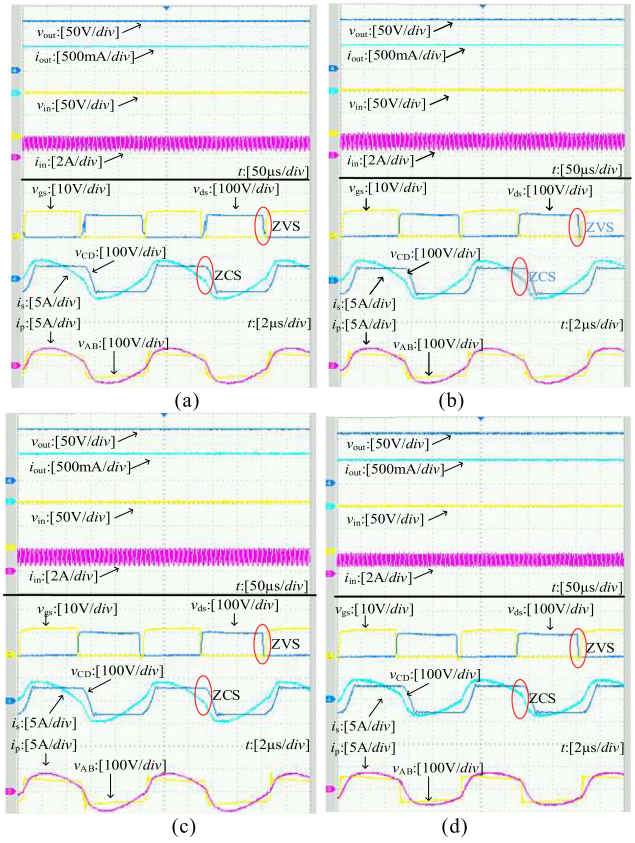

Fig. 17. Experimental waveforms when the primary side is offset along the x- and y-directions. (a) 5 mm in x-direction. (b) 10 mm in x-direction. (c) 5 mm in y-direction. (d) 10 mm in y-direction.

Considering that the working environment of the rotary transformer may cause an offset between the primary side and the secondary side due to vibration, it is also necessary to verify the performance on the anti-misalignment capability of the rotary transformer. Fig. 17 shows the waveforms when the primary side is shifted by 5 and 10 mm along the x and y directions inside the secondary side.

It can be seen from the Fig. 17 that the EMUCRT can still achieve ZVS ON the primary side of the transformer and ZCS ON the secondary side when the primary side is offset by 10 mm along the x-direction and the y-direction.

Compared with the SMUCRT, the comparison between the rotation angle θ and the transmission efficiency curve of the whole system is shown in Fig. 18(a). Under constant 100 V input and 100 kHz operating frequency and based on S/P compensation, the variation curves of the overall efficiency η of the EMUCRT system with the rotation angle θ, the x-direction offset at the same time are shown in Fig. 18(b). Considering that the offset of the original edge in the actual engineering cannot reach the length of the air-gap of 10 mm, 5 mm is taken as the maximum offset here.

Due to the cores on the secondary side of the EMUCRT wrap the cores on the primary side, the magnetic lines of force are more received by the secondary side and the coupling coefficient can be improved. It can be seen from Fig. 18(a) and (b) that

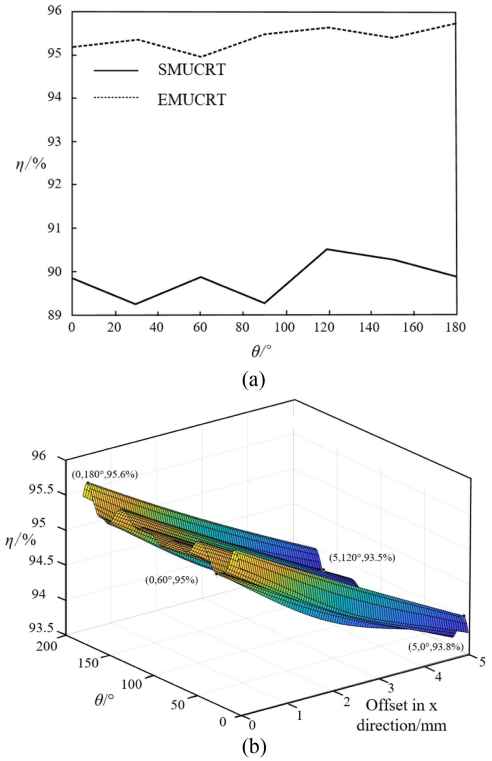

Fig. 18. Transmission efficiency curve of the whole system. (a) Comparison of efficiency curves of SMUCRT and EMUCRT during rotation. (b) With offset and rotation in the x-axis direction.

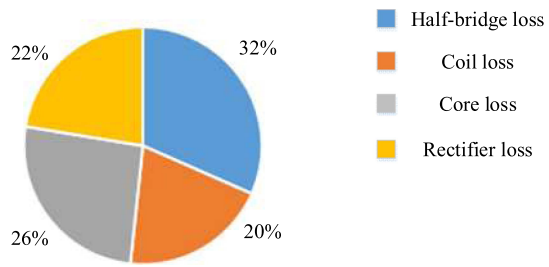

Fig. 19. Loss distribution of the system.

the efficiency of the EMUCRT is basically maintained at about 95%–95.6%, while the efficiency of the SMUCRT is stable at about 89.2%–90.3%. Therefore, the EMUCRT structure has higher rotational efficiency. In the case of offset the x-direction, when the maximum offset reaches 5 mm, the rotation efficiency of the whole machine can still reach 93.5%–93.8%, which is only about 2% lower than that without offset. So, it has relatively good anti-misalignment stability.

The total losses of the system are measured to be 6.83 W and the loss of the half-bridge inverter is 2.16 W. Meanwhile, the loss of the primary and secondary coils is 1.37 W. Core loss is calculated to be 1.77 W since it cannot be directly measured [24]. Finally, the loss of the rectifier is 1.53 W. Through comparative analysis, the specific proportion of each loss is obtained, as shown in Fig. 19.

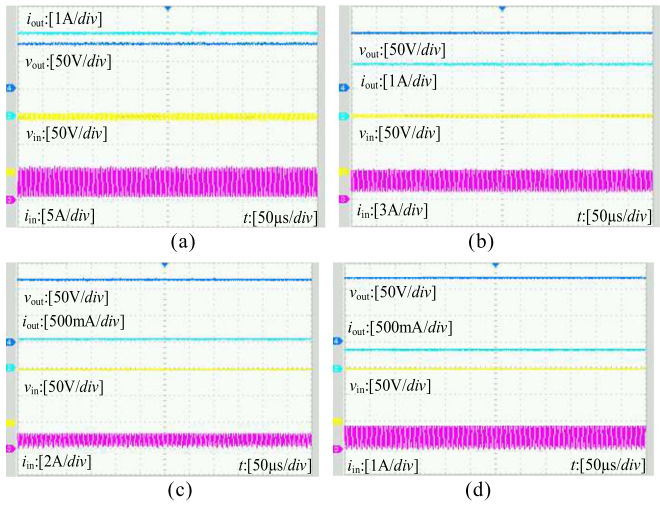

Fig. 20. Input and output waveforms under different loads. (a) 30% load. (b) Half load. (c) Full load. (d) 200% overload.

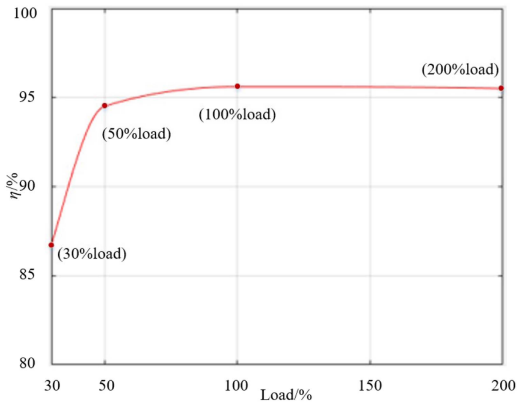

Fig. 21. Experimental curve of the variable load.

Considering that the light load or over load during the application process, it is necessary to discuss the system under variable load conditions, as shown in Fig. 20.

The final experimental curve of the overall efficiency with variable load is shown in Fig. 21.

The results show that the overall efficiency of the system remains basically stable in the range from half load to 200% overload. In the process of load reduction, the efficiency of the whole system is not greatly reduced, which is related to the characteristics of the compensation network. S/P compensation has superior load stability, so the system can adapt to a relatively wide variable load range.

The designed system in this article is compared with the existing rotary WPT systems, and the results are given in Table V.

It can be seen that the existing rotary transformers are generally characterized by low transmission efficiency and low air gap. Some structures even have problems such as lower efficiency when the rotation angle is different. So the structure designed by this article has the superiority of stable energy transmission.

TABLE V
PERFORMANCE COMPARISON OF EXISTING ROTARY WPT SYSTEM

Reference	Power/W	Operating frequency/ kHz	Gap/ mm	Efficiency /%
Method in [11]	1450	45	5	95
Method in [25]	20	520	2	89.7
Method in [26]	10	585	/	81
SMUCRT	100	100	10	90.3
EMUCRT	100	100	10	95.6

VI. CONCLUSION

In this article, an EMUCRT structure is proposed by improving the spliced magnetic core structure. In this structure, the primary magnetic core is embedded inside the secondary magnetic core, which effectively improves the coupling coefficient of the transformer and reduces the volume and weight of the system. Benefiting from the selection of the optimal magnetic core size and the combined splicing and embedded magnetic core structure, the proposed transformer structure can still ensure high transmission efficiency, good rotational stability and offset stability, and it could replace the conductive slip ring to supply power in some specific environments. Finally, an EMUCRT prototype is designed and established for experiment. The experimental results show good performance, verifying the success of the design and optimization.

REFERENCES

[1] R. Trevisan and A. Costanzo, "A 1-kW contactless energy transfer system based on a rotary transformer for sealing rollers," *IEEE Trans. Ind. Electron.*, vol. 61, no. 11, pp. 6337–6345, Nov. 2014.

[2] K. D. Papastergiou and D. E. Macpherson, "An airborne radar power supply with contactless transfer of energy—Part I: Rotating transformer," *IEEE Trans. Ind. Electron.*, vol. 54, no. 5, pp. 2874–2884, Oct. 2007.

[3] S. Zang, C. K. Yuan, C. James, and A. P. Hu, "Modular-Based PV system with contactless capacitive power transfer interface," in *Proc. IEEE PELS Workshop Emerg. Technol.: Wireless Power Transfer*, 2021, pp. 1–5.

[4] R. Chacko, M. H. Ravichandran, M. K. Sanoop, T. Sabu, V. T. Sadasivan Achari, and C. C. Joseph, "Magnetic slip ring—Rotary transformer based novel non-contact signal transfer mechanism for spacecraft application," in *Proc. Annu. Int. Conf. Emerg. Res. Areas, Magn., Mach. Drives*, 2014, pp. 1–5.

[5] X. Feng, Z. Fu, G. Hao, K. Wang, and Y. Weng, "Modeling and implementation of a new non-contact slip ring for wireless power transfer," in *Proc. IEEE 9th Int. Power Electron. Motion Control Conf.*, 020, pp. 106–111.

[6] Y. Zhang, J. Yang, D. Jiang, D. Li, and R. Qu, "Design of a contactless power transfer device with signal transmission," in *Proc. IEEE 22nd Int. Conf. Elect. Mach. Syst.*, 2019, pp. 1–5.

[7] S. Botha and N. Gule, "Design of a Contact-less energy transfer system for electrically excited synchronous machines," in *Proc. IEEE Int. Symp. Power Electron., Elect. Drives, Automat. Motion*, 2020, pp. 460–465.

[8] C.-S. Wang, O. H. Stielau, and G. A. Covic, "Load models and their application in the design of loosely coupled inductive power transfer systems," in *Proc. IEEE Int. Conf. Power Syst. Technol.*, 2000, vol. 2, pp. 1053–1058.

[9] Y. Luan, B. Lin, X. Ma, and X. Zhu, "Innovative contactless energy transfer accessory for rotary ultrasonic machining and its circuit compensation based on coil turns," *IEEE Trans. Ind. Electron.*, vol. 64, no. 10, pp. 7810–7818, Oct. 2017.

[10] X. C. Q. Chen, G. He, X. Ren, and S. -C. Wong, "Control scheme and characteristics analysis of three-phase series resonant converter suitable for contactless slipring system," in *Proc. IEEE Appl. Power Electron. Conf. Expo.*, 2017, pp. 2873–2879.

[11] G. He, Q. Chen, X. Ren, S. Wong, and Z. Zhang, "Modeling and design of contactless sliprings for rotary applications," *IEEE Trans. Ind. Electron.*, vol. 66, no. 5, pp. 4130–4140, May 2019.

[12] A. Kurs and R. Moffatt, and M. Soljacic, "Simultaneous mid-range power transfer to multiple devices," *Appl. Phys. Lett.*, vol. 96, no. 4, pp. 044102.1–044102.3, 2010.

[13] A. Sofia, A. C. Tavilla, R. Gardenghi, D. Nicolis, and I. Stefanini, "Power transfer for rotating medical machine," in *Proc. IEEE 38th Annu. Int. Conf. Eng. Med. Biol. Soc.*, 2016, pp. 2137–2140.

[14] T. Mizuno, S. Yachi, A. Kamiya, and D. Yamamoto, "Improvement in efficiency of wireless power transfer of magnetic resonant coupling using magnetoplated wire," *IEEE Trans. Magn.*, vol. 47, no. 10, pp. 4445–4448, Oct. 2011.

[15] A. Abdolkhani, A. P. Hu, and C. K. Nair, "Modelling and parameters identification of through-hole type wind turbine contactless sliprings," *Engineering*, vol. 4, no. 5, pp. 272–283, 2012.

[16] A. Esser and H.-C. Skudelny, "A new approach to power supplies for robots," *IEEE Trans. Ind. Appl.*, vol. 27, no. 5, pp. 872–875, Sep./Oct. 1991.

[17] M. Carpita, M. De Vivo, S. Gavin, and D. Bommottet, "A rotating contactless power transfer system for space applications," in *Proc. Int. Symp. Power Electron., Elect. Drives, Automat. Motion*, 2014, pp. 238–242.

[18] Y. Zhang, J. Yang, D. Jiang, D. Li, and R. Qu, "Design, manufacture, and test of a rotary transformer for contactless power transfer system," *IEEE Trans. Magn.*, vol. 58, no. 2, Feb. 2022, Art. no. 8400206.

[19] L. Y. song, W. S. han, L. B. jiang, Y. Y. fei, and L. Jun, "Performance comparison and analysis of rotary loosely coupled transformers with different structures," *Electrotechnical Appl.*, vol. 37, no. 08, pp. 46–52, 2018.

[20] K. Song et al., "A rotation-lightweight wireless power transfer system for solar wing driving," *IEEE Trans. Power Electron.*, vol. 34, no. 9, pp. 8816–8830, Sep. 2019.

[21] Z. Wei, C. Qian Hong, S. C. Wong, M. Tse, and C. Ling Ling, "Reluctance circuit and optimization of a novel contactless transformer," in *Proc. CSEE*, vol. 30, no. 27, pp. 108–116, Sep. 25, 2010.

[22] W. A. Roshen, "A practical, accurate and very general core loss model for nonsinusoidal waveforms," *IEEE Trans. Power Electron.*, vol. 22, no. 1, pp. 30–40, Jan. 2007.

[23] W. Goshen, "Ferrite core loss for power magnetic components design," *IEEE Trans. Magn.*, vol. 27, no. 6, pp. 4407–4415, Nov. 1991.

[24] D. Lin, P. Zhou, W. N. Fu, Z. Badics, and Z. J. Cendes, "A dynamic core loss model for soft ferromagnetic and power ferrite materials in transient finite element analysis," *IEEE Trans. Magn.*, vol. 40, no. 2, pp. 1318–1321, Mar. 2004.

[25] S. Ditze, A. Endruschat, T. Schriefer, A. Rosskopf, and T. Heckel, "Inductive power transfer system with a rotary transformer for contactless energy transfer on rotating applications," in *Proc. IEEE Int. Symp. Circuits Syst.*, 2016, pp. 1622–1625.

[26] C. Zhang, D. Lin, and S. Y. R. Hui, "Ball-Joint wireless power trans-fer systems," *IEEE Trans. Power Electron.*, vol. 33, no. 1, pp. 65–72, Jan. 2018.